Evaluation of an Orographic Precipitation Model

Idar Barstad* and Ronald B. Smith

Department of Geology and Geophysics, Yale University, New Haven, Connecticut

ABSTRACT

The question of whether rain gauge data from complex terrain are suitable to test physical models of orographic precipitation or to estimate free parameters is addressed. Data from three projects are considered: the Intermountain Precipitation Experiment (IPEX) and the California Land-falling Jets Experiment (CALJET), both in the United States, and the Mesoscale Alpine Programme (MAP) in the European Alps. As a prototype physical model, a new linear theory including airflow dynamics, condensed water advection, and leeside evaporation was employed. Theoretical considerations using the linear model showed sensitivity of point measurements across an ideal hill. To assist in model evaluation with real data, a new measure of "goodness of fit" was defined. This measure, "location sensitivity skill" (LSS), rewards detail as well as accuracy. For real data comparison, the linear model predictions show skill using traditional methods and the new LSS measure. The findings show that the wind direction and stability, and especially the cloud time delay (tau), are the sensitive parameters for point precipitation. The cloud time delay was the primary controller of point precipitation amplitude, and the stability tended to shift the precipitation pattern. Direct measures of tau are generally not obtainable, but this study indirectly constrained tau to 0–1000 s. The need for a denser observational network with tighter time control was revealed.

1. Introduction

One of the most challenging problems in weather forecasting is the quantitative prediction of precipitation. This challenge is even greater in regions with complex terrain where the ability to evaluate precipitation forecasts is significantly reduced due to nonrepresentative rain gauge sites and insufficient rain gauge density. This difficulty is unfortunate from a practical point of view, as forecasting of flash flooding, mudslides, erosion, water resources, and glacier mass budgets in mountainous terrain depends on accurate models.

At the same time, the subject of orographic precipitation has an inherent simplicity as a good part of the condensation is caused by forced ascent over fixed, well-known, terrain shapes (Charba et al. 2003). Orographic precipitation is a natural laboratory for cloud physics and dynamics (Rauber 1992). For this reason, in addition to its practical importance, the subject has received considerable attention (Smith 2004). A summary of proposed physical models is given in Table 1; see also

a review from the early 1990s by Barros and Lettenmaier (1994). As seen in the table, simple models have advanced over time. In parallel, the development of full numerical models has proceeded quickly, now offering a variety of "dynamical cores," cloud physics parameterizations, and methods for applying boundary and initial conditions (e.g., Hodur 1997). With all these models available, the question of model verification becomes more urgent. Model development without data constraint is inefficient and unproductive.

Data for evaluating precipitation models comes from two sources: 1) routine climatological rain gauge, radar, and streamflow measurements and 2) intense field programs with enhanced observing systems.

Model comparison with proxy methods such as stream gauges, which is inferred from area-integrated precipitation, involves an additional model to handle runoff delays (Jasper and Kaufmann 2003), adding uncertainties. Radar information is often truncated by shielding terrain (White et al. 2003), and in addition there are problems such as refraction, particularly for short-wave radars. Even in more traditional rain gauge networks, the accuracy might be poor because of factors like the airflow around the collector (Yang et al. 1998). In snow drift cases this is particularly true (H. Olafsson 2003, personal communication).

Over the last three decades, many targeted field programs have been carried out around the globe, for example in the European and New Zealand Alps, and in

* Current affiliation: Geophysical Institute, University of Bergen, Bergen, Norway.

Corresponding author address: Idar Barstad, Geophysical Institute, University of Bergen, Allegt. 70, 5007 Bergen, Norway.
E-mail: idar@gfi.uib.no

TABLE 1. A selection of orographic precipitation models showing the evolution throughout the years. An empirical precipitation efficiency factor (PE factor) is often used to limit the precipitation. In the second column, raw upslope is the vertical velocity constant with height, simple is the linear reduction with height to the level of no vertical motion, linear wave is the linear gravity wave theory, and numerical solves equations numerically.

References	Airflow dynamics	Cloud physics	Remarks
Fraser et al. (1973); Hobbs et al. (1973)	2D, linear wave	Sophisticated	Ice phase only
Collier (1975)	Simple	Drift only	
Colton (1976)	2D, ?	Drift only	PE factor
Rhea (1978); Hay and McCabe (1998)	Simple	Drift only	PE factor
Smith (1979)	Raw upslope	Instant	
Alpert and Shafir (1989)	Raw upslope	Drift, diffuse	PE factor
Haiden et al. (1990)	Simple	Conversion, drift	
Oki et al. (1991)	Nonlinear, numerical	Instant	PE factor
Barros and Lettenmaier (1993)	3D, linear wave	Instant	PE factor; see various extensions in the literature
Sinclair (1994)	Simple	Instant	PE factor
Smith (2003)	Raw upslope	Linear, conversion and drift	Tune with terrain smoothing
Kunz (2003)	3D, linear wave	Conversion and drift	PE factor
Smith and Barstad (2004)	3D, linear wave	Linear, conversion and drift	Tune with time delay
Colle et al. (1999); Mass et al. (2002)	Nonlinear, numerical	Sophisticated	Full numerical model

the Cascade, Sierra, and Wasatch Ranges in the western United States. In this paper, we focus on conventional point precipitation data from three field programs: the Intermountain Precipitation Experiment (IPEX; Schultz et al. 2002), the California Land-falling Jets Experiment (CALJET; Ralph et al. 1998), and the Mesoscale Alpine Programme (MAP; Bougeault et al. 1997, 2001). Thus, our work can be put in a context of more complete observations and analysis (sections 4–6). For a prototype model, we choose the linear theory of Smith and Barstad (2004) as it is simple to apply and has a small set of free parameters. A similar exercise could be undertaken with any other simple or full numerical model.

This paper is organized as follows. A brief outline of the linear model development is found in section 2. In section 3 we investigate the sensitivity of point data to model parameters. In section 4, we introduce a new statistical measure of model performance. In section 5 we create a synthesized dataset and test if we are able to infer the uncertain input parameters to the model. We also show how errors in the data make this inference of input parameters more difficult. In section 6, we test the model against data from three field projects. Section 7 summarizes our results.

2. The linear theory of orographic precipitation

As a prototype physical model, we use the linear steady-state theory of orographic precipitation proposed by Smith and Barstad (2004). A key component of the model is the advection of vertically integrated condensed water [$q_c(x,y)$ = cloud water density and $q_f(x,y)$ = hydrometeor density] written as

$$\mathbf{U} \cdot \boldsymbol{\nabla} q_c = S(x, y) - q_c/\tau_c \quad \text{and} \qquad (1a)$$

$$\mathbf{U} \cdot \boldsymbol{\nabla} q_f = q_c/\tau_c - q_f/\tau_f, \qquad (1b)$$

where τ_c and τ_f are the constant characteristic time scales for cloud water conversion and hydrometeor fallout and S the source term of cloud water. See Table 2 for further explanation of variables. If airflow dynamics is neglected, S in (1a) can simply be $S(x,y) = \rho_{v0}\mathbf{U} \cdot \boldsymbol{\nabla} h(x, y)$ [i.e., the raw upslope model from Smith (1979)], where ρ_{v0} is the average water vapor density at the surface and $\boldsymbol{\nabla} h$ the terrain slope. As lifting in front of a mountain drives S positive, the sink in (1a) acts in (1b) as a source, and (1b) has precipitation [$P(x,y) = q_f/\tau_f$] as the final sink to the system; S gets the opposite sign in downslope regions. Negative precipitation gen-

TABLE 2. Some explanation of symbols used in the linear model.

Name	Symbol	Typical values
Terrain elevation	h(x,y)	1–2000 m
Intrinsic frequency; k and l are respective wavenumbers	$\sigma = Uk + Vl$	0.01–0.0001 s^{-1}
Horizontal wind; U and V are respective components	$\mathbf{U} = U\mathbf{i} + V\mathbf{j}$	1–50 m s^{-1}
Moist stability frequency	N	0–0.01 s^{-1}
Water vapor scale height	H_w	1–5 km
Conversion time	τ_c	200–2000 s
Fallout time	τ_f	200–2000 s
Uplift sensitivity factor: ρ_{v0} = surface water vapor density, γ = environmental lapse rate, Γ = moist-adiabatic lapse rate	$C_w = \rho_{v0}\gamma/\Gamma$	0.001–0.02 kg m^{-3}
Background precipitation rate	P_∞	0–5 mm h^{-1}
Vertical wavenumber	m	0.01–0.0001 m^{-1}

erated in strong downdrafts is unphysical and is truncated away.

These equations, and the airflow dynamics equations, can be solved using Fourier transforms to obtain

$$\hat{P}(k, l) = \frac{C_w i\sigma \hat{h}(k, l)}{(1 - imH_w)(1 + i\sigma\tau_c)(1 + i\sigma\tau_f)} \quad \text{and} \quad (2)$$

$$P(x, y) = \int\int \hat{P}(k, l)e^{i(kx+ly)}dkdl + P_\infty. \quad (3)$$

The symbols in (2) and (3) are described in Table 2. The first parenthesis in the denominator in (2) describes how the source term is modified by airflow dynamics. The two remaining parentheses in (2) describe the advection of condensed water during conversion and fallout. The model reduces to the raw upslope model when $H_w = \tau_c = \tau_f = 0$ and $C_w = \rho_{v0}$. See Smith and Barstad (2004) for further detail about the model.

The pattern and amount of precipitation predicted by (2) is controlled primarily by two types of nondimensional parameter. First is the nondimensional moist layer depth, $\tilde{H} = NH_w/U$, where U is the magnitude of the wind. Large values of $\tilde{H}$ reduce the amount of condensation as the uplift does not penetrate the moist layer. The condensation is also shifted upstream due to gravity wave tilt. The other type of control parameter is the nondimensional cloud drift time $\tilde{\tau} = U\tau/a$, where a is the mountain half-width. Large values of $\tilde{\tau}$ indicate that condensed water will drift onto the lee slopes and evaporate, instead of converting and falling on the windward slopes. For the purpose of simplifying the analysis, we have set the two tau values equal throughout this paper. A discussion of this approach may be found in Smith and Barstad (2004).

3. Parametric sensitivity of point precipitation

In this section, we show how sensitive point precipitation is to the governing parameters in a physical model. The insight gained here will help in the real analyses to follow.

The sensitivity of precipitation to $\tilde{\tau}$ and $\tilde{H}$ is displayed by mapping out the parameter space defined by these numbers for a specific point. An isolated circular Gaussian mountain with half-width $a = 20$ km is chosen as the underlying topography. In linear theory the mountain height (h_m) is a multiplier rather than a control parameter. The parameter space for three chosen points across the centerline of the mountain are shown in Fig. 1: (a) the upslope point, (b) the mountain peak, and (c) the downslope point. The precipitation values are normalized with the raw upslope value ($\tilde{\tau} = 0$, $\tilde{H} = 0$) for the upslope point ($x = -a$).

Point a has its maxima, equal to unity (i.e., the raw upslope value), close to its origin in Fig. 1a. As the moist layer deepens (increased $\tilde{H}$), the forced ascent is unable to penetrate and condense vapor at all levels.

As the cloud time delay (i.e., $\tilde{\tau}$) increases, the precipitation is advected downstream of point a. A minor effect, barely seen in Fig. 1, is the increase in precipitation with $\tilde{\tau}$ for large moist layer depth. The tilted wave requires a larger $\tilde{\tau}$ to carry precipitation back to the windward slope station.

For point b at the hilltop, the maximum is shifted to $\tilde{\tau} \sim 0.4$ and is slightly reduced because of the smoothing effect from the increased tau. As the condensation source function is maximum upstream of point a, considerable advection is required to bring precipitation to point b. In Fig. 1b, we also see the effect of the tilted wave. As the moist layer depth increases, a greater cloud delay is necessary to counteract the effect of upstream wave tilt.

Precipitation at point c has a much smaller magnitude and its sharp maximum is located around $\tilde{\tau} = 2$. The sharp gradient just below unity is due to drying aloft above the mountain peak caused by the wave dynamics. Only for mountain widths comparable to or less than $U\tau$ will precipitation particles spill over to point c on the lee side.

4. Measures of model skill

The skill of a model must be judged from a statistical measure. Various scores and skills may be found in the literature. Textbooks by Wilks (1995) and Jolliffe and Stephenson (2003) provide an introduction to forecast verification. A shorter text by Nurmi (2003) gives a nice review of the various measures and their capabilities. See also the overview by Jasper and Kaufmann (2003).

Some studies have assigned precipitation observations to intervals—so-called stratification by precipitation—evaluated by various score and skill measures (Wilks 1995; Colle et al. 1999). Stensrud and Wandishin (2000) presented a summary of various measures and proposed a correspondence ratio in the evaluation of forecasts. Their measure is an extension of the well-known threat score and, therefore, requires stratification of the compared fields. Cherubini et al. (2002) presented upscaling techniques as an alternative to point-precipitation-based evaluation. Typically measures like root-mean-square error (rmse; see definitions below) and bias (bias) are involved in the evaluation. We shall see in section 5 that models having very detailed fields are normally penalized more harshly than smooth models for inaccuracies. This might explain why increased resolution in numerical models is not rewarded proportionally (Mass et al. 2002). To mitigate this, we will add another measure to our evaluation approach.

The traditional spatial error estimates such as rmse and bias are defined as

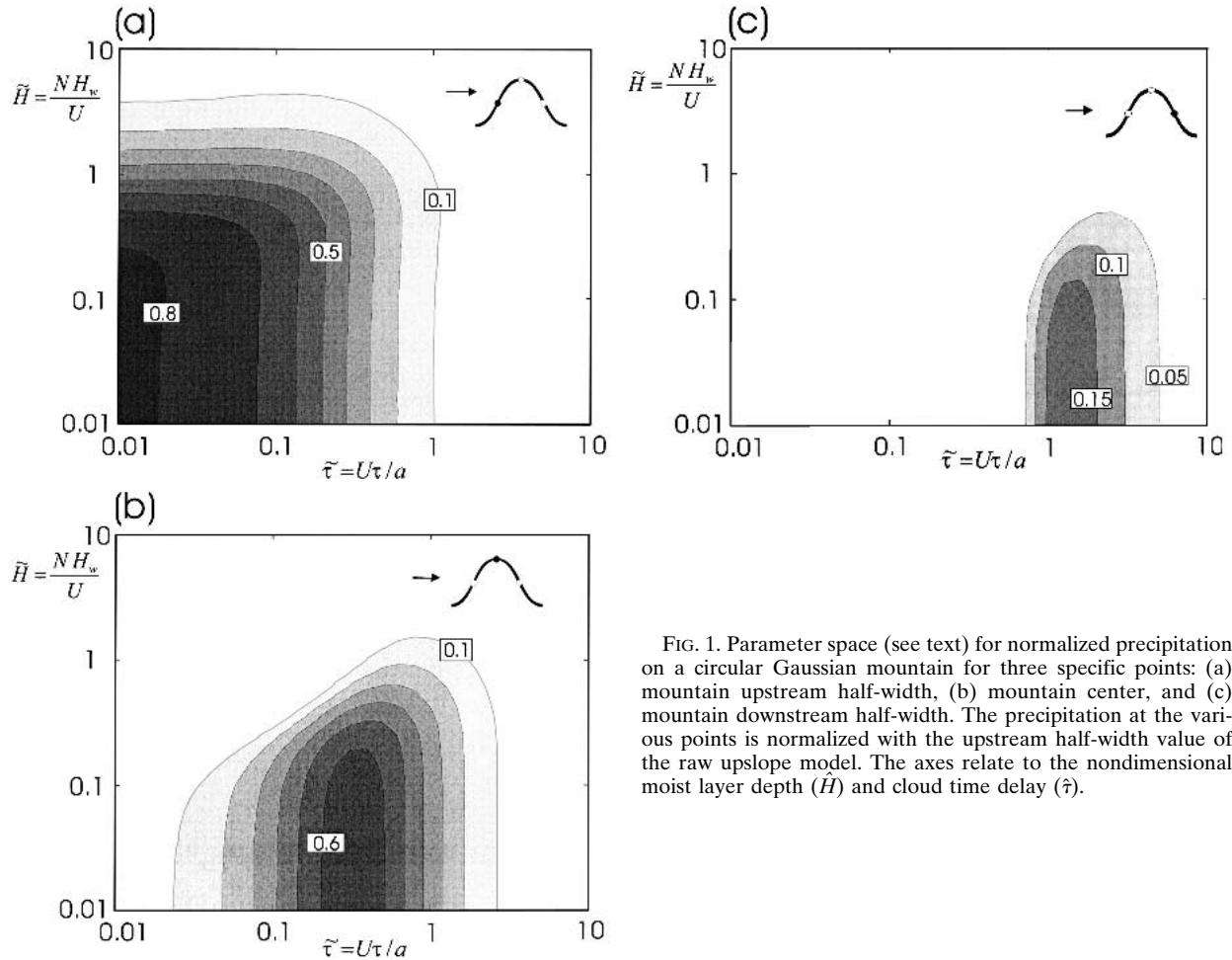$$\text{rmse} = \sqrt{\frac{1}{n}\sum_{i=1}^{n}(P_i - O_i)^2} \quad \text{and} \quad (4)$$

FIG. 1. Parameter space (see text) for normalized precipitation on a circular Gaussian mountain for three specific points: (a) mountain upstream half-width, (b) mountain center, and (c) mountain downstream half-width. The precipitation at the various points is normalized with the upstream half-width value of the raw upslope model. The axes relate to the nondimensional moist layer depth ($\hat{H}$) and cloud time delay ($\hat{\tau}$).

$$\text{bias} = \frac{1}{n} \sum_{i=1}^{n} (P_i - O_i), \qquad (5)$$

where n is the number of samples, and P_i and O_i are the predicted and observed samples, respectively (Wilks 1995).

A deficiency of a measure often used in the evaluation of models can easily be illustrated using a regular Pearson correlation (Wilks 1995); imagine two series made up of random numbers. The correlation is near zero. By smoothing one of the series, the correlation improves. Measures without constraints on the level of details are in danger of favoring smoother fields. We prefer statistical measures that give credit for both details and accuracy, particularly as we deal with orographic precipitation characterized by large spatial variability. This will encourage the development of detailed models. For these reasons, we propose a new measure called location sensitivity skill (LSS).

Calculation of the LSS is done by testing the error estimates E (e.g., bias and rmse) when station locations are moved randomly around within an assigned radius

($r_{\max}$) from the correct location. Numbers from a random generator determine the angle and distance from the correct location within $r_{\max}$; see illustrations in Fig. 2. The maximum radius is steadily increased and the error estimate is repeatedly recalculated. Ideally, the
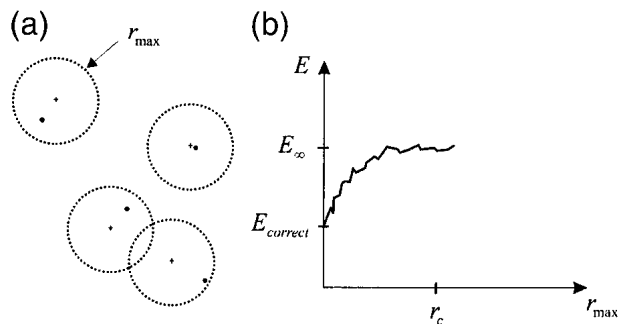

FIG. 2. Schematic drawing of how the location sensitivity skill (LSS) works. (left) An assigned maximum radius ($r_{\max}$) constrains the "new" location (dot) of the station. (right) A schematic picture of how the error estimate (E) is a function of $r_{\max}$; E_∞ is evaluated at r_c. See text for further explanations.

error increases as we move away from the station, and it eventually flattens out (E_∞; see Fig. 2). We define the LSS as

$$\mathrm{LSS} = 1 - \frac{E_{\mathrm{correct}}}{E_\infty}. \tag{6}$$

In a smooth-field case, the locations of the stations do not matter, and errors do not change with increasing radius, and (6) gives zero skill. Whereas when the correct location error in (6) is small and E_∞ is big (i.e., a detailed model field with high accuracy), the skill is closer to unity.

As a practical matter, one must cut off the LSS calculation at some finite radius, r_c (Fig. 2). In this paper we have chosen r_c to be 40 km where the error flattens out. In the terrains we have investigated, LSS change little beyond that cutoff. Any improvement in E beyond this limit is not expected to be explained by model physics ($U\tau < r_c$).

5. Parameter inference from synthesized data

There are several uncertain parameters in the linear model system—first of all, the cloud time delay factors, which are set equal, $\tau = \tau_c = \tau_f$, to simplify our approach. Previous estimates of tau vary from 200 to 2000 s (Smith 2003; Smith et al. 2005). Additionally in complex terrain, the overall wind direction may not be accurately known. A small change in wind direction (dd) might influence the resulting point precipitation (Nuss and Miller 2001; Ralph et al. 2003). Point precipitation is also sensitive to stability (N) and background precipitation (P_∞). The main goal for this section is to see if the underlying parameters (τ, dd, N, P_∞) can be detected through the minimization of errors. We will focus on the (τ, dd) space and we will test the minimization procedure when errors (discrepancies between model and observation data) are added to the fields.

a. Uncertain input variables—Microphysics and wind direction

To test how different error estimates such as rmse and bias can be used to infer the correct values of parameter pairs such as (τ, dd), we use the linear model to create a synthesized dataset for a given topographic area with real station locations. We chose to use 73 rain gauge sites in the Lago Maggiore area (northern Italy), which is the same network used later in the paper for an investigation of a real MAP case (see section 6c). The τ was varied from 0 to 2000 s at 100-s intervals. The wind direction (dd) was changed from 180° to 155° at 6.25° intervals. The other input variables were kept fixed and are those of MAP IOP2b. The arbitrarily defined reference condition had dd = 167.5° and τ = 600 s.

Figure 3a shows how rmse changes as a function of two uncertain input parameters (τ, dd). Good convergence to the correct values of dd and τ is seen. The
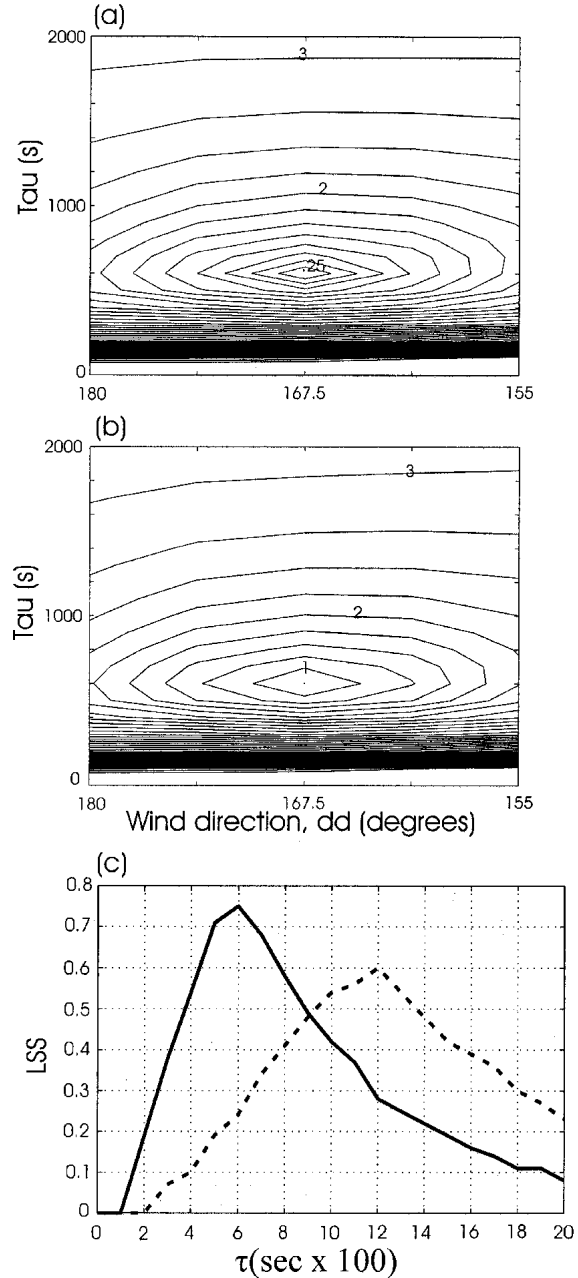

FIG. 3. Contours of error measure (rmse) as a function of the uncertain parameters (dd and τ) in the linear model system. (a) The rmse is shown when the correct input parameters are set to be (dd = 167.5°, τ = 600 s). (b) As in (a) but with error added to the observations, where the error amplitude A = 4. (c) LSS optimum for correct τ = 600 s (solid line) and τ = 1200 s (broken line) when A = 4.

strongest gradient in rmse is found for tau values shorter than the reference. The maximum amplitudes in rmse along the x axis at tau = 600 s are about ± 1.75 mm h^{-1}.

If the reference τ is assumed to be 1200 s, the gradient in rmse is considerably weaker, and the correct lo-

cation in (τ, dd) parameter space does not stand out as clearly (not shown).

For example the bias, a measure of the systematical error, does not give as good result as the rmse in the minimization (not shown). For very short tau, the detail level increases and the amount of truncated negative precipitation is enhanced. For longer tau, the pattern does not necessarily show a monotonic increase away from the correct tau.

Using the rmse, we have undertaken tests similar to those in Fig. 3a, but with other parameter pairs (P_∞, τ) and (N, τ). The results are not shown. If P_∞ varies from 0 to 2 mm on the x axis and tau is similar to that in Fig. 3a, then the variation in rmse is ± 0.75 mm h^{-1} along the x axis at the correct τ. For N a stronger dependency is found; the rmse variation is about ± 1.75 mm/h^{-1} when N varies from 0.001 to 0.005 s^{-1} on the x axis.

b. Errors in observation networks

We define errors as either additive or multiplicative. An additive error might be caused by a thunderstorm or embedded convection in the area, violating the assumptions of the model. A multiplicative error might be an uncertainty in wind direction or a proportional rain gauge error.

The multiplicative error might be written as

$$O^i = T^i \varepsilon^i = T^i A \, \text{Rand}^i_{0-1} \quad O^i \in (0, AT^i), \quad (7)$$

where O^i is a single observation and T^i its true value, A is the error amplitude factor, and Rand^i_{0-1} denotes a random number between 0 and 1. The observation is scaled with the true value. When $A = 2$, the distribution of O^i is within the range 0–2, and the bias eliminates for large n is

$$\frac{1}{n} \sum_{i \to n} O^i \to \frac{1}{n} \sum_{i \to n} T^i. \quad (8)$$

For other values of A this is not true.

An additive error might be expressed as

$$O^i = \text{Max}(T^i + \varepsilon^i, 0)$$
$$= \text{Max}(T^i + A\text{Rand}^i_{-0.5-0.5}, 0) \quad O^i \in (0, T^i + A/2).$$
$$(9)$$

Since the additive error is not scaled with the true value, we must use a max function to avoid negative values of precipitation. For $A \leq 2$, we ensure that the max function is redundant, as negative values in (9) cannot occur. Since the random number in (9) is centered around 0, the bias will be zero (i.e., 8) when the max function is redundant. Larger values of A do not meet this requirement, and (8) is not satisfied.

c. Inferring dd and tau from datasets containing errors

As described in section 5b, errors are added to the synthesized dataset for a reference run (dd = 167.5°

and $\tau = 600$ s) and the results for the additive ($A = 4$) error are shown in Fig. 3b. For multiplicative error, the results give similar trends (not shown). We have prepared Table 3 to show how big the error amplitude (A) can be while we still are able to recover the correct location in various parameter spaces. Results for N, P_∞, and dd versus τ are given for both $\tau = 600$ and 1200 s. In the table, simulations with longer correct taus (1200 s) have greater difficulties identifying the correct tau due to smoother fields. Just as in section 5a, the bias estimate is not a good measure for inferring the correct location in various parameter spaces due to convergence problems in the minimization. This result may not be surprising based on (8) and the discussion that followed.

d. Inferring tau from datasets containing errors: Using LSS

Figure 3c shows the minimization procedure repeated, but using LSS to identify the correct tau value. The only free parameter in the figure is tau, and two sets of minimizations are shown (600 s, indicated with a solid line, and 1200 s, indicated with a dashed line). The figure shows that LSS has a crisp definition of the correct underlying tau values with errors added ($A = 4$). When the correct underlying tau is 1200 s, the signal is weaker having a less sharp gradient. For larger A, the maxima are proportionally less. For $A = 20$, the LSS shows only small values (around 0.1 for $\tau = 1200$ s and 0.25 for $\tau = 600$ s) and has problem in focusing at the correct τ.

It is difficult to specify an error amplitude A for real data. Nevertheless, this analysis is meant to build confidence in the inference of unknown parameters. Likewise, it is meant to identify the most sensitive input parameters next after τ. We conclude that the determination of model parameters by rmse minimization is possible under some but not all circumstances. The LSS measure appreciates details in another way than rmse, and when errors are added to the data, the LSS assists in finding the correct τ. In the following, we anticipate τ to be the main free parameter.

TABLE 3. For various free parameters (N, P_∞, dd), how capable are rmse and bias minimization in retrieving underlying variable as the error amplitude (A) becomes larger? The yes/no (Y/N) answer this question for tau = 600 s/1200 s. See text for further explanation.

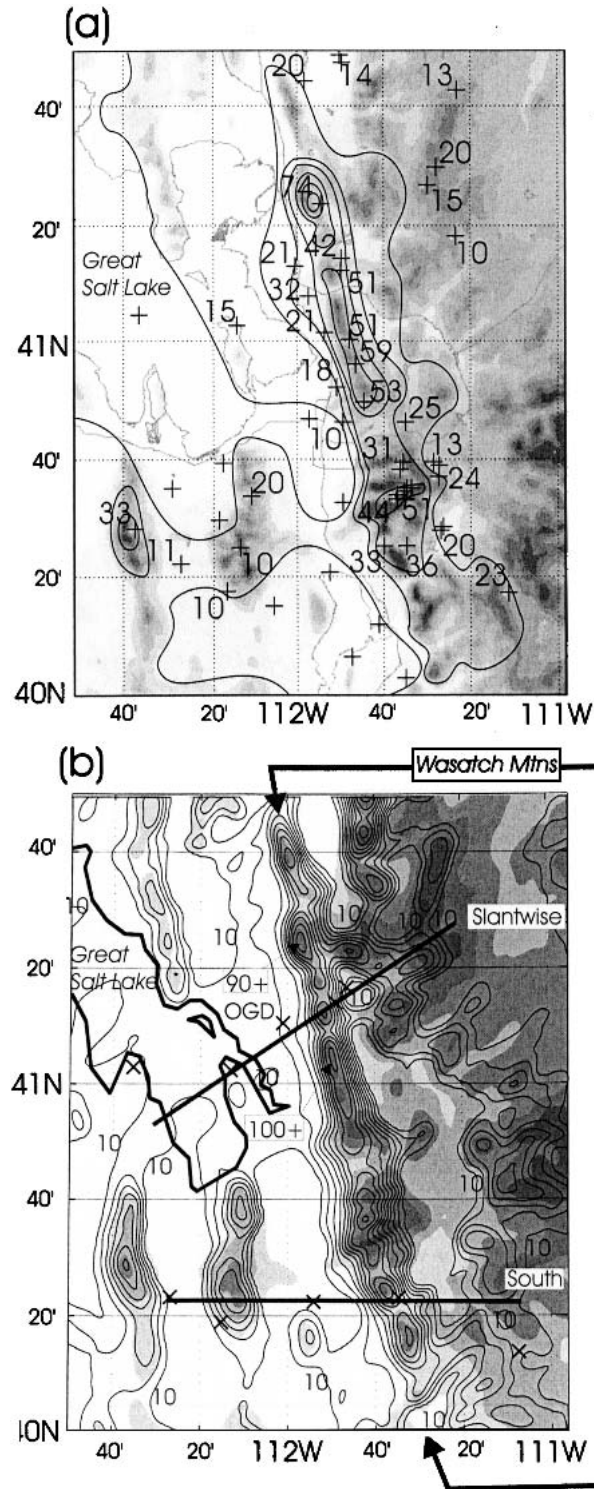|	N		P_∞		dd	
A	Rmse	Bias	Rmse	Bias	Rmse	Bias
0	Y/Y	Y/Y	Y/Y	Y/Y	Y/Y	Y/Y
2.5	Y/Y	N/N	Y/Y	N/N	Y/Y	N/N
5	Y/Y	N/N	Y/N	N/N	Y/Y	N/N
7.5	Y/Y	N/N	Y/N	N/N	Y/N	N/N
10	Y/Y	N/N	N/N	N/N	Y/N	N/N
15	Y/N	N/N	N/N	N/N	Y/N	N/N
20	N/N	N/N	N/N	N/N	N/N	N/N

FIG. 4. The Wasatch Mountains located to the east of Great Salt Lake received heavy precipitation due to winds from the west-southwest during IPEX-IOP3. (a) Observations with hand-drawn isolines of total precipitation for IOP3 with contours every 10 mm. The figure is taken from Cheng (2001). (b) Linear model prediction for 12-hourly precipitation in mm with contours every 10 mm. The τ was set to 500 s and $N = 0.005$ s^{-1}. A light smoothing on short-wave length (less than 800 m) is applied on the terrain

6. Comparing with real data

Data from three field campaigns have been used to constrain the main free parameter. In order to have control of the temporal evolution, we have sought data with high temporal resolution. Although the chosen cases are quasi-steady state, we have averaged hourly records to limit the amount of model runs and the amount of data to compare.

a. IPEX IOP3

The Intermountain Precipitation Experiment (IPEX) campaign was undertaken in Utah, in the western United States, 2000 (Schultz et al. 2002). The intensive observing period (IOP3) (0600 UTC 12 February–0600 UTC 13 February) stood out as the most significant orographic precipitation event in this campaign (Cox et al. 2005). The 12-h period from 1300 UTC 12 February to 0100 UTC 13 February included most of the precipitation in IOP3. Generally, the wind direction changed from south-southwest to more west-southwesterly during the intense precipitation period. Balloon soundings were issued every third hour, and the soundings at Ogden (OGD; see Fig. 4) in the Wasatch Mountains and at Oasis (LMR) about 100 km upstream (Figs. 4 and 11 in Cox et al. 2005), show that the wind had a shifting behavior with height. Judging from the 1735 UTC sounding at LMR, the wind was more westerly in a layer around 600 hPa, and an along-barrier jet was weakening throughout the event. The soundings showed a small (0–3 K) dewpoint depression and weak moist stability, (Schultz et al. 2002). During IPEX, 37 reliable rain gauges reported hourly in the Oquirrh and Wasatch Mountains located east and south of Great Salt Lake. In addition, the National Oceanic and Atmospheric Administration (NOAA) P3 aircraft flew several missions along the mountain ridge, scanning with its X-band tail radar. We judge the number of rain gauges and their distribution to be insufficient to support a full statistical analysis, so we used a direct comparative approach.

Figure 4a shows the hand-drawn isolines for accumulated precipitation for the whole event (Cheng 2001). Correspondingly, Fig. 4b shows the simulated precipitation pattern for the most intense 12-h period. The input parameters were wind speed = 12.5 m s^{-1} from the west-southwest (dd = 240°), $N = 0.003$ s^{-1}, $T_0 = 278$ K, and $\tau = 500$ s. The input values (T_0, dd, and wind speed) are based on the LMR/OGD soundings. Comparing the two panels in Fig. 4, we see that the overall precipitation pattern seems to be nicely reproduced. The predicted amounts compared to the hand-drawn

←

(shaded) to avoid artificial high-frequency waves. The two heavy lines indicate vertical cross sections shown in Fig. 5.

isohyets are too big. This may indicate that a longer tau is more appropriate. It may also be that the locations of the observations constituting the hand-drawn map were such that the largest amounts of precipitation were missed. The dry areas downstream of the mountain crest can be seen in both fields. Weak precipitation upstream of the mountain foothills in the linear model caused by the upstream tilt in the wave dynamics is also seen.

The radar cross section taken from the P3 shows that the main orographic cloud extends 10–15 km upstream from the crest, and the thinner cloud layer extends to about 20 km upstream; see Fig. 9 in Schultz et al. (2002; information available online at www.nssl.noaa.gov/teams/ipex/iop3). The radar cross section perpendicular to the ridge shows an abrupt cutoff of the main orographic cloud at the crestline. This is associated with descent and evaporation on the lee side of the Wasatch Mountains. This cutoff matches well what we see from Fig. 4; the main precipitation is located near the peak of the mountain, about $2*U\tau = 20$ km downstream of the condensation source region.

Whereas Fig. 4b shows results from a single model run, Figs. 5a,b depict the sensitivity of the precipitation to input variables N and τ. Five observations are located in the vicinity of each cross section indicated in Fig. 4. The station locations are projected into cross-sectional planes, and the hourly precipitations are shown in Figs. 5a,b. The linear model is run for five different sets of parameters based on a reference run ($\tau = 500$ s, $N = 0.003$ s^{-1}). The τ (250, 500, and 750s) and

the N (0.001, 0.003, 0.005 s^{-1}) are varied, but the wind stays fixed. From Fig. 5, we see that the precipitation rates are most sensitive to the chosen tau value, particularly for small values. The larger tau values reduce the peak precipitation significantly and shift it from just upstream to just downstream of the peaks. Immediately upstream of the station labeled SNM in Fig. 5a, a large drop in precipitation is seen as tau increases from 250 to 500 s. This rapid drop with increasing tau is reminiscent of Fig. 1b for $\tilde{\tau} = U\tau/a \approx 0.75$. The pattern is much less sensitive to static stability.

All the model runs underpredict the precipitation at stations in the valley west of the Wasatch front. Precipitation at these stations came primarily in the early part of the IOP, having more southerly winds, which is a possible explanation for the discrepancy.

According to our test in section 5a, the variation in wind direction might also change this picture. However, the Wasatch Range is more ridgelike, reducing direction sensitivity.

b. CALJET

CALJET took place in California, in 1997/98. Neiman et al. (2002) studied the precipitation's sensitivity to wind speed perpendicular to the coastal mountains for different locations along the Californian coast. The advantage of this project is the availability of hourly cross-shore wind components from wind profilers and hourly precipitation for three profiler–rain gauge "couplets" (northern, central, and southern couplet). The flows were divided into two categories: blocked and
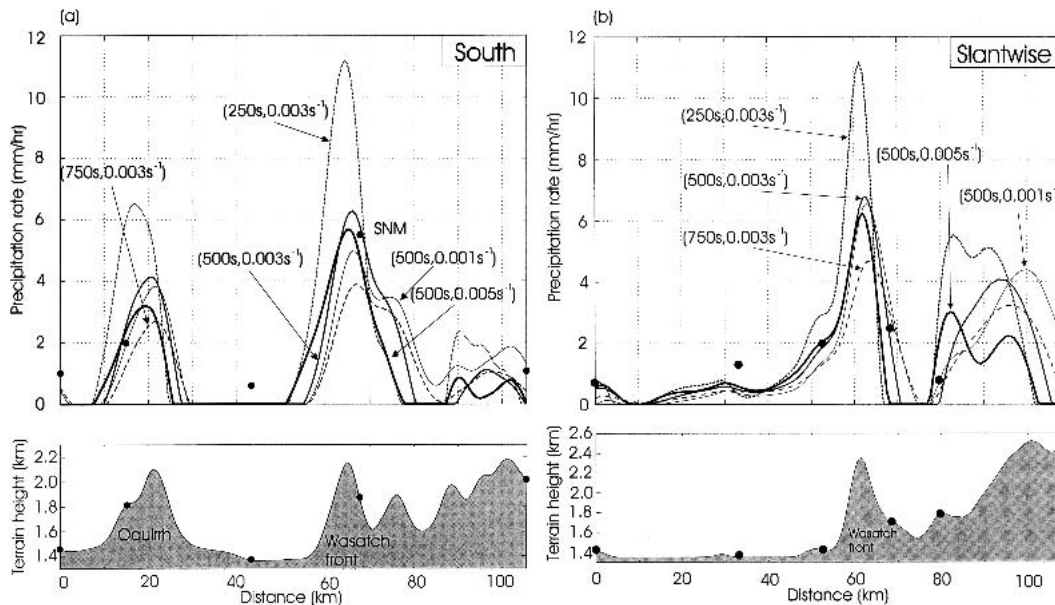

FIG. 5. (top) Precipitation rate and (bottom) terrain height for (a) the W–E Wasatch cross section and (b) the slantwise SW–NE cross section indicated in Fig. 4. The points are observed precipitation values and lines are linear model results. The solid lines are simulations with $\tau = 250$ s (short dashed), 500 s (solid), and 750 s (long dashed line) and various $N = 0.001$ s^{-1} (thin), 0.003 s^{-1} (medium), 0.005 s^{-1} (heavy line). The other parameters stayed fixed.

nonblocked flow situations. We only consider the latter in this paper. The rain gauges are located between the upslope and ridge top; so Figs. 1a and 1b are both helpful in understanding the response to changing environments.

According to Figs. 3 and 5 in Neiman et al. (2002), both cases discussed for the southern and northern couplets had southwesterly (SW) winds during the significant precipitation period. For the northern couplet, the SW winds only reached 2 km, with westerlies prevailing aloft. Both locations have overall ridgelike mountains and a line perpendicular to the ridgeline surrounding the northern station points at 230°, 5° from the flow direction. For the southern stations a perpendicular line points to 190°, 35° from the flow direction. The rain gauge station is located halfway up the slope, similar to the ideal geometry in Fig. 1a. The stability of the flow was reported to be near neutral; accordingly, we show runs with weak stability: $N = (0.001, 0.002, 0.003)$ s^{-1}. The surface temperature was inferred from reported equivalent potential temperature and is set to $T_0 = 288$ K.

We show results from the linear model for the northern and the southern rain gauge stations in Fig. 6. We see that the reduction mechanisms in the linear model (airflow dynamics and slow cloud physics) generally reduce the raw upslope model (heavy solid line) to give improved agreement with the data. This is particularly true at the northern rain gauge station (Fig. 6a). For both stations, the start of precipitation is shifted off from $U = 0$ as the wind speed increases.

Figure 7 shows a cross section along the flow for condensation and precipitation for two wind speeds for the northern station. The station is located at the origin of the x axis. Note that the precipitation curves are smoother and shifted downwind from the condensation curves. Inspection of Fig. 7 reveals that condensation produced at the main lifting upstream from the station will only hit the station for appropriate $\tilde{\tau}$. The lower wind speed case is on the very verge of moistening the station. For the southern station, a peak of condensation is found immediately upstream, and weak winds (small $\tilde{\tau}$) bring precipitation to the station (not shown). The northern station may have generally deeper vertical penetration than the southern station because the flow impinging on the ridge at a right angle instead of from the side. For stronger winds we expect full penetration of the moist layer (small $\tilde{H}$), but more of the condensate is advected past the stations (larger $\tilde{\tau}$), limiting the precipitation. The sensitivity to stability in Fig. 6 suggests that the effective stability of the air masses sensed by the airflow is higher than $N = 0.003$ s^{-1}.

We have also investigated the central couplet case, but results are not displayed. In this case, the wind direction is more south-southwesterly and the model results favor an explanation that this was a more neutral case with rather short taus (about 250 s).
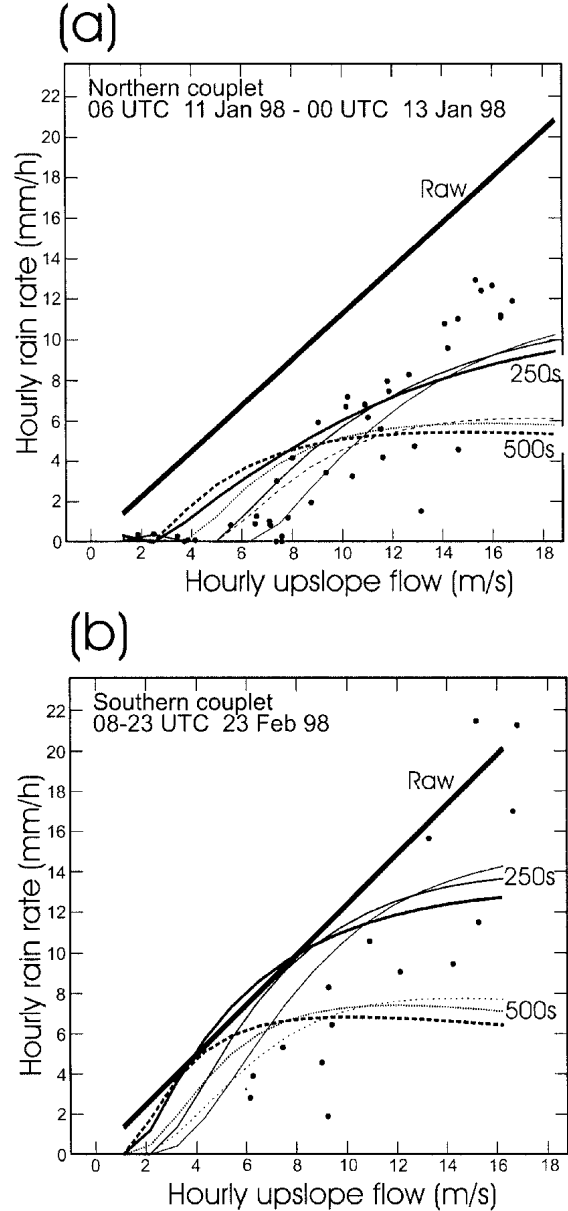

FIG. 6. Points are observed hourly precipitation rates from CALJET mountain stations in the (a) Sonoma area (38.61°N, 123.21°W) referred to as the northern station, and (b) Santa Barbara area (34.51°N, 119.85°W) referred to as the southern station, both in California. Data are taken from Neiman et al. (2002). Lines indicate the linear model values at the station locations for $\tau = 250$ s (solid lines) and $\tau = 500$ s (broken lines). The stabilities are $N = (0.001, 0.002, 0.003)$ s^{-1}, where the stronger stability has the thinner line. The heavy solid line indicates the results from the raw upslope model.

c. MAP: IOP2b and IOP8

The MAP took place in the fall season of 1999 in the central southern Alps. The density of conventional rain gauge observations as well as observation of other atmospheric parameters was enhanced, both in time and
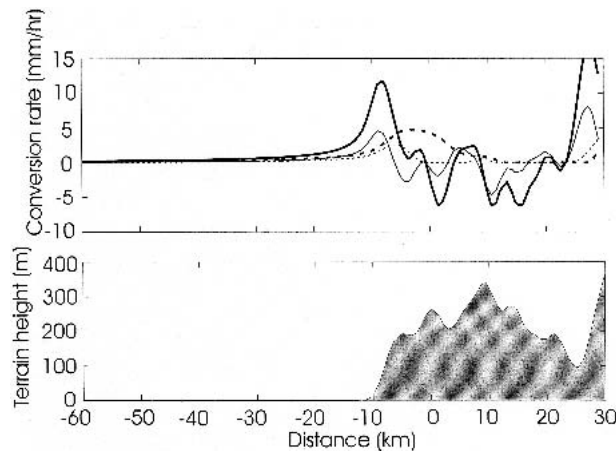
FIG. 7. Vertical cross section intersecting the northern rain gauge station at the origin of the x axis. The direction of the cross section is aligned with the flow direction (SW). Condensation (solid lines) and precipitation (broken lines) are shown for two wind speeds—$U = 10$ m s^{-1} (heavy lines) and $U = 5$ m s^{-1} (thin lines) perpendicular to the coast. The model terrain is shown in the lower panel.

in space. The rain gauge density and the amount of data push for using the statistical evaluation methods discussed in section 4.

During MAP, two heavy rain events (IOP2b and IOP8) provided a good opportunity for studying orographic precipitation, using 73 stations for IOP2b and 59 for IOP8 reporting hourly in the Lago Maggiore area. The characteristics of the atmospheric parameters for these two events were different. IOP2b was warm ($T_0 = 287$ K in our model run) and nearly unstable case with some embedded convection, while IOP8 was cold ($T_0 = 278$ K), stable, and had some low-level blocking (Rotunno and Ferretti 2003). For both cases, the wind direction comes from the southeast sector (IOP8 had the largest easterly component), and the wind speed at 850 hPa was between 12 and 20 m s^{-1} during the most intense precipitation.

To simplify the comparison between the model and the observations, we estimated one representative observation value for each station. This is done by averaging the time series for the most intense precipitation period, and giving a single value for each station. The averaging procedure tends to smooth the field, but is a necessity to reduce our data and for our assumption of a steady state. The most intense precipitation period is found from the average precipitation values for the stations in the area (45°–47°N, 8°–10.5°E). The model data are interpolated to the station location for comparison.

The goal of our Alpine analysis is twofold: first, to compare the linear theory and raw upslope models, and second, to estimate the value of the cloud time delay. We have prepared Tables 4–7 to show how the two models perform as the main free parameters change. The raw upslope model has terrain smoothing as the

TABLE 4. Precipitation statistics for IOP2b in the Lago Maggiore area: measure of goodness for the linear model as the characteristic time scale of conversion and fallout of hydrometeors (τ) increases. The observed station mean is 3.0 mm h^{-1}. See text for definitions of error estimates.

τ (s)	Avg (mm h^{-1})	Bias (mm h^{-1})	Rmse (mm h^{-1})	LSS$_{rmse}$
0	5.4	2.4	10.1	0.04
250	4.1	1.1	5.5	0.00
500	2.7	−0.3	3.7	0.03
750	2.5	−0.5	2.9	0.08
1000	2.6	−0.4	2.5	0.10
1500	2.8	−0.2	2.1	0.09
2000	2.7	−0.3	1.9	0.05
3000	2.3	−0.7	1.8	0.03
4000	1.9	−1.1	1.9	0.02

free parameter and the linear model has τ as the free parameter.

1) MAP: IOP2B

In IOP2b, the 16-h period 0600–2200 UTC 20 September 1999 had the most intense precipitation. During this period, the wind profiler at the Lenate airport (Rotunno and Ferretti 2003) showed a steady wind, approximated to $U = 15$ m s^{-1} from dd $= 167.5°$. The surface temperature was set 5° lower ($T_0 = 287$ K) than the value observed at Milano airport (292 K) to avoid moist instability. As an example of the linear model performance of IOP2b, we have prepared Fig. 8a, showing hourly precipitation rates. In addition to the parameters above, we have set $\tau = 500$ s and $N = 0.003$ s^{-1}. The simulated pattern and amount may be compared with maps of observations in Rotunno and Ferretti (2003, Fig. 3); and in Medina and Houze (2003), their Fig. 6. The overall simulated pattern and amounts seem to be well reproduced.

With increasing tau, the station–averaged precipitation in Table 4 decreases. In general, this decrease is caused by "carryover" and increased lee-slope evaporation. The accuracy of the linear model is poor (high bias and rmse) when only the dynamics in the model is included (i.e., $\tau = 0$). For $\tau = 1000$s, we get the best

TABLE 5. Precipitation statistics for IOP2b in the Lago Maggiore area: measure of goodness for the raw upslope model as smoothing increases. The observed station mean is 3.0 mm h^{-1}. See text for definitions of error estimates.

Smoothing (km)	Avg (mm h^{-1})	Bias (mm h^{-1})	Rmse (mm h^{-1})	LSS$_{rmse}$
0.8	8.4	5.4	17.6	0.2
2	5.9	2.9	8.9	0.16
3	5.4	2.4	7.0	0
4	4.9	1.9	6.0	0
5	4.6	1.6	5.0	0
10	3.9	0.9	3.0	0.04
20	3.1	0.1	2.5	0.05

TABLE 6. Precipitation statistics for IOP8 in the Lago Maggiore area: measure of goodness for linear model as the characteristic time scale of conversion and fallout of hydrometeors (τ) increases. The observed station mean is 1.7 mm h^{-1}. See text for definitions of error estimates.

τ (s)	Avg (mm h^{-1})	Bias (mm h^{-1})	Rmse (mm h^{-1})	LSS$_{rmse}$
0	7.6	5.9	14.4	0.06
250	2.1	0.5	3.8	0
500	1.1	−0.6	1.8	0.01
750	0.9	−0.8	1.4	0.04
1000	0.9	−0.8	1.3	0.09
1500	0.9	−0.8	1.3	0.07
2000	0.9	−0.8	1.3	0.05
3000	0.9	−0.8	1.4	0.03
4000	0.8	−0.9	1.5	0.01

overall results (bias = −0.4, rmse = 2.5, LSS = 0.1) with a relatively high level of spatial detail and rather low error. Rmse continues to decline for larger tau, but assuming there are errors in the data (see discussion in section 5), we trust LSS's sharper definition of the optimum tau.

In Table 5, we repeat the same statistical procedure for the raw upslope model, with the terrain smoothing as the free parameter. The model behaves rather poorly. With little smoothing, the bias and rmse are very large. LSS shows some skill, in part because the field is full of small-scale details. With more smoothing, the bias and rmse decrease, but remain too high. The LSS shows little skill and is incapable of suggesting an optimum value for smoothing.

A cross section from the linear model runs with various tau values along 8.425°E is shown in Fig. 9a. Nearby observations averaged over the intense precipitation period are indicated with crosses and the associated standard deviation in time are indicated as vertical lines. The observations near the first elevation in the south of the cross section tend to vary a lot in time. In this case, contributions of embedded convection are likely (Yuter and Houze 2003).

2) MAP: IOP8

The later event (IOP8) lies in another flow regime; colder and more stable air giving a tendency for stag-

TABLE 7. Precipitation statistics for IOP8 in the Lago Maggiore area: measure of goodness for the raw upslope model as smoothing increases. The observed station mean is 1.7 mm h^{-1}. See text for definitions of error estimates.

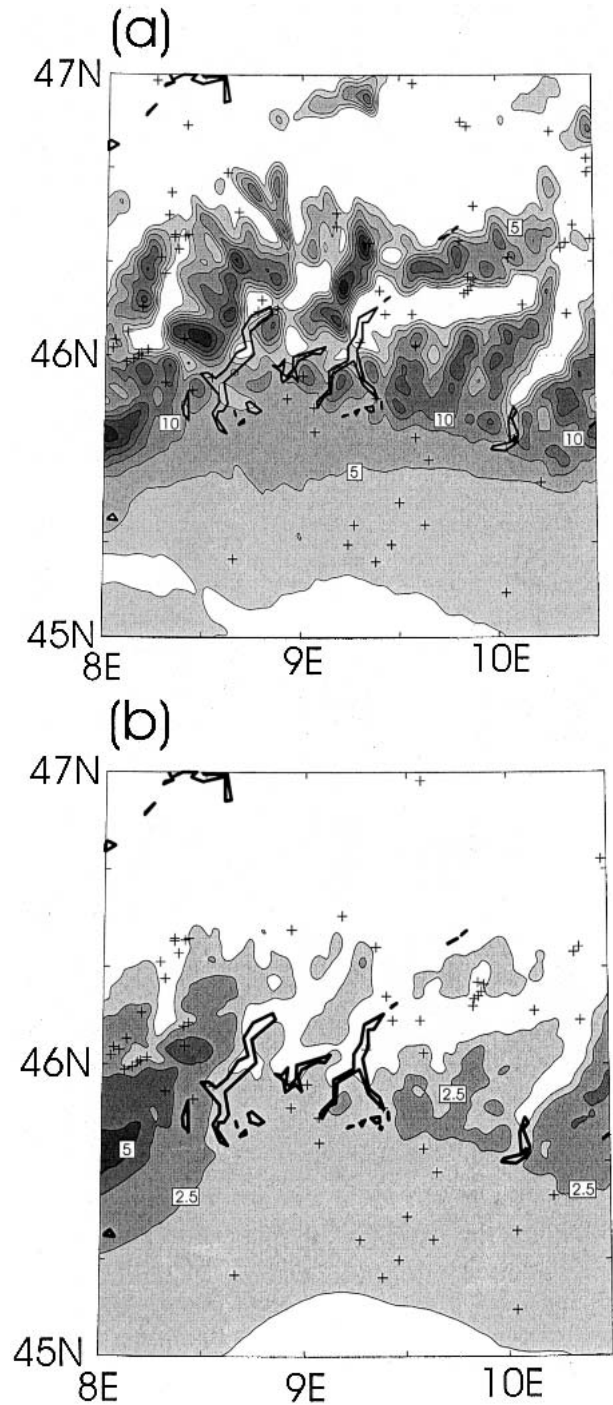| Smoothing (km)	Avg (mm h^{-1})	Bias (mm h^{-1})	Rmse (mm h^{-1})	LSS$_{rmse}$
0.8	7.9	6.2	15.3	0.26
2	6.1	4.4	9.5	0.05
3	5.5	3.8	7.5	0
4	5.0	3.4	6.4	0
5	4.7	3.0	5.6	0
10	3.7	2.1	3.4	0
20	2.7	1.1	2.0	0.03

FIG. 8. Hourly precipitation rate simulated by the linear model for the Lago Maggiore area in northern Italy during MAP, where crosses indicate station locations: (a) IOP2b with 2.5 mm h^{-1} contours and (b) IOP8 with 1.25 mm h^{-1} contours. Heavy contours indicate water bodies.

nation. Due to the lack of convection, we expect different microphysical behavior in this case (Yuter and Houze 2003). The intense period of precipitation lasts about 18 h (0200–2100 UTC 21 October 1999). Figure
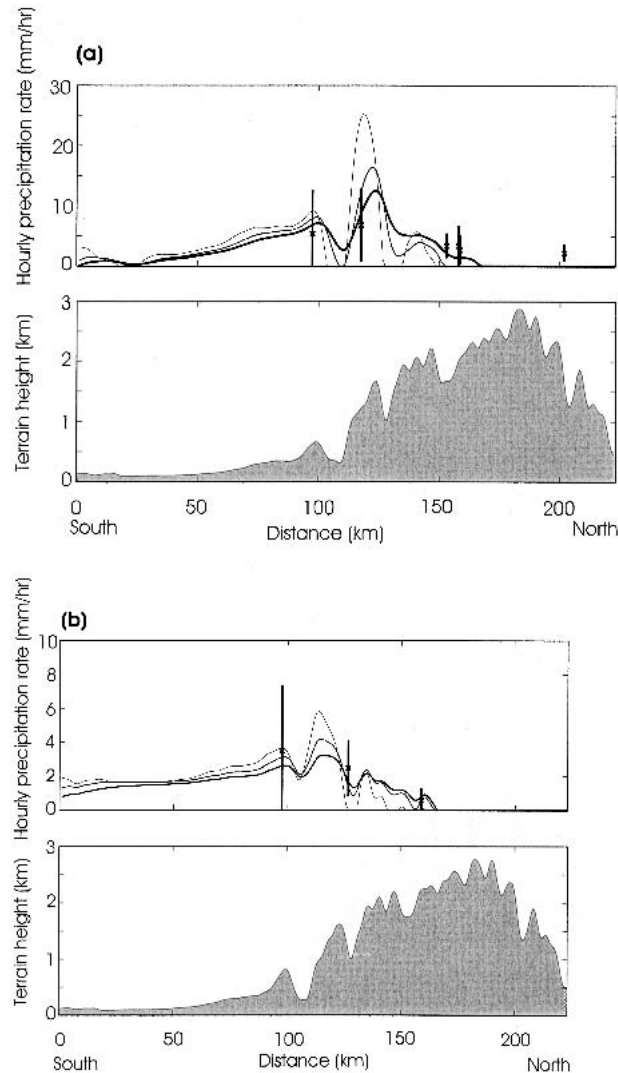
FIG. 9. (top) Cross section of simulated hourly precipitation along a longitude in Fig. 8. Three runs with various taus are depicted. The thinner line corresponds to the shortest tau. Nearby averaged hourly observed precipitation rates are indicated with crosses, and the standard deviations for the respective stations are indicated with vertical lines; see text for further explanation. (bottom) The terrain along the cross section. (a) IOP2b with cross section along 8.425°E showing the closest stations within the range (8.35°–8.5°E). Runs with tau equal to 250 s (thinner), 500 s, and 750 s (thicker) are shown. Other input variables are equal to the run in Fig. 8a. (b) For IOP8, the cross section is taken at 8.433°E showing stations from the range (8.41°–8.46°E). The tau values are 500 s (thinner), 750 s, and 1000 s (thicker).

8b shows hourly precipitation results from the linear model simulation with input parameters $\tau = 1000$ s, dd $= 135°$, $U = 18$ m s^{-1}, and $N = 0.01$ s^{-1}.

Tables 6 and 7 show how the skill of the two models changes as free parameters are changed. In most respects, the error patterns in IOP8 are similar to those in IOP2b. For the linear theory, the best cloud time delay is about 1000 s. This value gives small bias and rmse and the maximum LSS = 0.09.

The raw upslope model performs poorly as before. With little smoothing, it gives a highly detailed precipitation pattern with very large bias and rmse, but substantial LSS. When smoothing is applied, the bias and rmse improve, but LSS no longer suggests any pattern skill.

Figure 8b shows the linear model cross section for IOP8 along 8.433°E. Also here, the standard deviation of the southernmost station is large. This indicates a non-steady-state behavior, which makes the interpretation of our results more difficult.

3) THE LINEAR MODEL RESULTS IN COMPARISON TO RESULTS FROM THE OTHER IOPS: STUDIES OF THE MAP CAMPAIGN

IOP2b and -8 in the MAP campaign have been the subject of several studies (e.g., Medina and Houze 2003; Rotunno and Ferretti 2003; Bousquet and Smull 2003; Smith et al. 2003; Yuter and Houze 2003; Georgis et al. 2003; Asencio et al. 2003). For IOP2b, Georgis et al. (2003) noted that rain over the mountains was homogeneous with quasi-stationary vertical development, whereas over the plain upstream, the rain was characterized with convective periods. The general understanding from the cited papers is that convection contributed to the large amount of precipitation in IOP2b. Rotunno and Ferretti (2003) showed that stronger-stability low-level blocking in IOP8 pushed the rain pattern further upstream and caused a more widespread precipitation similar to what we see in Fig. 8. We note that the linear model applied in this paper predicts these rainfall amounts reasonably well, with no special treatment of convection or blocking. The surface temperature was set conservatively, limiting the influx of water vapor. The linear model suggests that the discrepancies between the two cases are first of all due to surface temperature and perhaps only secondarily due to static stability differences.

d. Similarities and differences in the three case studies

Orographic precipitation cases are seldom characterized by steady-state conditions. Both microphysics and wave dynamics are likely to change with time. In this study, we have picked quasi-steady events with a rather tight time control to reduce the number of required model runs. In particular, the MAP campaign data have been averaged in order to compare observations with single model runs. The single model runs have allowed us to discuss the mechanisms in the linear model to a greater extent.

The linear design of the model favors cases characterized by linear mechanisms and with weak to moderate stably stratified air (no convection or stagnation). In this study we found indications that the nonlinearity of the microphysics is important in explaining the large discrepancy for strong winds in warm air (CALJET).

Although we have no direct information about the microphysics in the investigated cases in CALJET, White et al. (2003) documented frequent cases without bright-bands (most likely warm rain cases) during the winter season the experiment took place. Thus by inspection of a simple warm rain scheme in a numerical model (Klemp and Wilhelmson 1978), we see that the formulation of cloud water collection by raindrops ($C_r = k\, q_{cl}\, q_r^{0.875}$, where k is a constant, q_{cl} the mixing ratio of cloud water, and q_r the mixing ratio for rainwater) results in increased nonlinearity as the cloud/rainwater content increases. In warm air, increased wind speed definitely provides more condensate (Jiang and Smith 2003). A positive nonlinearity would give a shorter tau in fast, moist winds. The data in CALJET would show a better fit if the stability was increased a little beyond $N = 0.003\ \mathrm{s}^{-1}$ and tau was shortened for high wind speeds.

In the IPEX case, a bright band was found (Cox et al. 2005) at lower altitudes. A bright band was also found in MAP IOP2b and IOP8, at 3.5 and 2 km, respectively (Yuter and Houze 2003). Accordingly, the drift of solid hydrometeors above the bright bands was significantly longer than for the CALJET cases. This might be part of the reason why the τ's for these cases were found to be longer than for the CALJET-cases.

Generally, we suspect several of the studied cases have a varying tau. For a CALJET–northern couplet (Fig.6a), it seems like the clusters of observations indicate two different microphysical regimes. We are not able to confirm this because we lack microphysical information about the specific observations in the clusters. Moreover, in the Alpine analysis both IOP's seem to have a similar microphysical behavior judging from the tau values. However, the cold MAP case (IOP8) might have a longer drift of hydro meteors, and shorter conversion time, and the IOP2b just the opposite. A two-layered linear model distinguishing air masses above and beneath the melting layer might address this problem.

Several of our case studies had measurements indicating near-neutral stability. Our theoretical approach in section 3 and Jiang (2003) was to show clearly that precipitation is sensitive to stability. Flows over mountains often include large latent heat releases altering the stability. Overturning by convection may have a similar role. There is no easy way to quantify a bulk stability for such flows. In CALJET, we found indications, such as an offset of precipitation from $U = 0$ and suggestions from the data to increase the stability, that some stability is sensed by the flow. On the other hand, a threshold in the microphysics might be an alternative explanation for the offset.

The model–data comparison in MAP was based on an average of hourly precipitation records. At least for some stations, large variations were hidden inside the averaging, particularly near the upwind foothills. Even if we had used the 1-h sampling frequency to the full

extent in a smaller area, we would have no guarantee against hidden important structures within the data (Yuter and Houze 2003). The question of what is the natural time scale for various orographic precipitation cases arises.

7. Summary and conclusions

In this paper we have identified challenges in evaluating an orographic precipitation model such as (i) poor data coverage, (ii) errors in the observations, and (iii) uncertainty in the model input variables, and (iv) misleading statistical measures of goodness. We have considered the sensitivity of point precipitation to governing physical parameters in the orographic precipitation problem, especially the cloud time delay. We have also defined a new estimate of the model skill (LSS) that takes into account the pattern detail of the model field. While the LSS values found are not impressive, they seem to assist in finding an optimum value of cloud time delay. In future field projects, a denser observation network with tighter time control will allow us to explore the capability of the LSS measure.

Data from three field experiments have been used to test the linear model and to constrain its parameters. A summary of cloud time delays is shown in Table 8. Generally, tau values in the range up to 1000 s are supported by our analysis.

We are not satisfied with the accuracy of our tau estimates, nor do we think that tau values will be the same in every location or event. Even within the same storm, tau might vary. The tau's value is important, however, as it summarizes the practical effect of cloud physics processes. Our results suggest that future observation and modeling projects should try to estimate the cloud delay parameters and the role of condensed water drift and downslope evaporation. Perhaps future projects could independently estimate τ_c and τ_f. In general, existing rain gauge networks are not well suited to this endeavor. Models, including the linear model, may be used to identify critical observation points and strong gradient regions where measurements could best be added to estimate the cloud delay parameters and test model performance. We have seen that the cloud time delay primarily controls the precipitation amplitude and to some extent shifts the precipitation pattern.

TABLE 8. Project summary. The third column refers to the microphysics. "Estimated tau" refers to the best-fit values inferred.

Project	Type of data		Regime	Estimated tau (s)
	Time	No. of stations		
IPEX	12 h	37	Cold	500–1000
CALJET	hourly	2, including wind profilers	Warm?	200–500
MAP 2b	16 h	73	Cold	<1000
MAP 8	18 h	59	Cold	<1000

The stability has a second-order effect, primarily shifting the precipitation pattern, particularly for wider mountains. By deploying rain gauges such that we are able to catch the maxima and the gradients found downstream crestlines (cf. Figs. 1 and 5), we are more suited to determine tau and stability in events. As inflow conditions may change rapidly, experiments with tight time control are needed.

REFERENCES

Alpert, P., and H. Shafir, 1989: Meso-gamma-scale distribution of orographic preciption: Numerical study and comparison with precipitation derived from radar measurements. *J. Appl. Meteor.,* **28,** 1105–1117.

Asencio, N., J. Stein, M. Chong, and F. Gheusi, 2003: Analysis and simulation of local and regional conditions for the rainfall over the Lago Maggiore Target Area during MAP IOP2b. *Quart. J. Roy. Meteor. Soc.,* **129B,** 565–586.

Barros, A. P., and D. P. Lettenmaier, 1993: Dynamic modeling of the spatial distribution of precipitation in remote mountainous areas. *Mon. Wea. Rev.,* **121,** 1195–1214.

——, and ——, 1994: Dynamic modeling of orographically induced precipitation. *Rev. Geophys.,* **32,** 265–284.

Bougeault, P., and Coauthors, 1997: MAP Mesoscale Alpine Programme design proposal. MAP Programme Office, 77 pp. [Available from MAP Programme Office, c/o Swiss Meteorological Institute, Krähbülstrasse 58, CH-8044 Zürich, Switzerland.]

——, and Coauthors, 2001: The MAP special observing period. *Bull. Amer. Meteor. Soc.,* **82,** 433–462.

Bousquet, O., and B. F. Smull, 2003: Observations and impacts of upstream blocking during a widespread orographic precipitation event. *Quart. J. Roy. Meteor. Soc.,* **129B,** 391–409.

Charba, J. P., D. W. Reynolds, B. E. McDonald, and G. M. Carter, 2003: Comparative verification of recent quantitative precipitation forecasts in the National Weather Service: A simple approach for scoring forecast accuracy. *Wea. Forecasting,* **18,** 161–183.

Cheng, L., 2001: Validation of quantitative precipitation forecast during the Intermountain Precipitation Experiment. M.S. thesis, Dept. of Meteorology, University of Utah, 137 pp.

Cherubini, T., A. Ghelli, and F. Lalaurette, 2002: Verification of precipitation forecasts over the Alpine region using a high-density observing network. *Wea. Forecasting,* **17,** 238–249.

Colle, B. A., K. J. Westrick, and C. F. Mass, 1999: Evaluation of MM5 and Eta-10 precipitation forecasts over the Pacific Northwest during the cool season. *Wea. Forecasting,* **14,** 137–154.

Collier, C. G., 1975: A representation of the effects of topography on surface rainfall within moving baroclinic disturbances. *Quart. J. Roy. Meteor. Soc.,* **101,** 407–422.

Colton, D. E., 1976: Numerical simulation of the orographically induced precipitation distribution for use in hydrologic analysis. *J. Appl. Meteor.,* **15,** 1241–1251.

Cox, J. A. W., W. J. Steenburgh, D. E. Kingsmill, J. C. Shafer, B. A. Colle, O. Bousquet, B. F. Smull, and H. Cai, 2005: The kinematic structure of a Wasatch Mountain winter storm during IPEX IOP3. *Mon. Wea. Rev.,* in press.

Fraser, A. B., R. C. Easter, and P. V. Hobbs, 1973: A theoretical study of the flow of air and fallout of solid precipitation over mountainous terrain. Part I: Airflow model. *J. Atmos. Sci.,* **30,** 801–812.

Georgis, J.-F., F. Roux, M. Chong, and S. Pradier, 2003: Triple-Doppler radar analysis of the heavy rain event observed in the Lago Maggiore region during MAP IOP 2b. *Quart. J. Roy. Meteor. Soc.,* **129B,** 495–522.

Haiden, T., P. Kahlig, M. Kerschbaum, and F. Nobilis, 1990: On the influence of mountains on large-scale precipitation: A deterministic approach towards orographic PMP. *Hydrol. Sci.,* **35-5,** 501–510.

Hay, L. E., and G. J. McCabe, 1998: Verification of the rhea-orographic-precipitation model. *J. Amer. Water Res. Assoc.,* **34,** 103–112.

Hobbs, P. V., R. C. Easter, and A. B. Fraser, 1973: A theoretical study of the flow of air and fallout of solid precipitation over mountainous terrain. Part II: Microphysics. *J. Atmos. Sci.,* **30,** 813–823.

Hodur, R. M., 1997: The Naval Research Laboratory's Coupled Ocean/Atmosphere Mesoscale Prediction System (COAMPS). *Mon. Wea. Rev.,* **125,** 1414–1430.

Jasper, K., and P. Kaufmann, 2003: Coupled runoff simulations as validation tools for atmospheric models at the regional scale. *Quart. J. Roy. Meteor. Soc.,* **129B,** 673–692.

Jiang, Q., 2003: Moist dynamics and orographic precipitation. *Tellus,* **55A,** 301–316.

——, and R. B. Smith, 2003: Cloud timescale and orographic precipitation. *J. Atmos. Sci.,* **60,** 1543–1559.

Jolliffe, I. T., and D. B. Stephenson, Ed., 2003: *Forecast Verification: A Practitioner's Guide in Atmospheric Sciences.* John Wiley, 240 pp.

Klemp, J. B., and R. B. Wilhelmson, 1978: The simulation of three-dimensional convective storm dynamics. *J. Atmos. Sci.,* **35,** 1070–1096.

Kunz, M., 2003: Simulation von Starkniederschlagen mit langer Andauer uber Mittelgebirgen. Ph.D. thesis, University of Karlsruhe, 170 pp.

Mass, C. F., D. Ovens, K. Westrick, and B. A. Colle, 2002: Does increasing horizontal resolution produce more skillful forecasts? *Bull. Amer. Meteor. Soc.,* **83,** 407–430.

Medina, S., and R. A. Houze, 2003: Air motions and precipitation growth in Alpine storms. *Quart. J. Roy. Meteor. Soc.,* **129B,** 345–371.

Neiman, P. J., M. Ralph, A. B. White, D. E. Kingsmill, and P. O. G. Persson, 2002: The statistical relationship between upslope flow and rainfall in California's coastal mountains: Observations during CALJET. *Mon. Wea. Rev.,* **130,** 1468–1492.

Nurmi, P., 2003: Recommendations on the verification of local weather forecasts. ECMWF Tech. Memo. 430, Reading, United Kingdom, 19 pp.

Nuss, W. A., and D. K. Miller, 2001: Mesoscale predictability under various synoptic regimes. *Nonlinear Proc. Geophys.,* **8,** 429–438.

Oki, T., K. Musiake, and T. Koike, 1991: Spatial rainfall distribution at a storm event in mountainous regions, estimated by orography and wind direction. *Water Resour. Res.,* **27,** 359–369.

Ralph, F. M., and Coauthors, 1998: The use of tropospheric profiling in the California Land-Falling Jets Experiment (CALJET). *Proc. Fourth Int. Symp. on Tropospheric Profiling: Needs and Technologies,* Aspen, CO, University of Colorado, 258–260.

——, and Coauthors, 2003: The impact of a prominent rain shadow on flooding in California's Santa Cruz Mountains: A

CALJET case study and sensitivity to the ENSO cycle. *J. Hydrometeor.,* **4,** 1243–1264.

Rauber, R., 1992: Microphysical structure and evolution of a central Sierra Nevada orographic cloud System. *J. Appl. Meteor.,* **31,** 3–24.

Rhea, J. O., 1978: Orographic precipitation model for hydro-meteorological use. Ph.D. thesis, Colorado State University Atmospheric Paper 287, 198 pp.

Rotunno, R., and R. Ferretti, 2003: Orographic effects on rainfall in MAP cases IOP2b and IOP8. *Quart. J. Roy. Meteor. Soc.,* **129B,** 373–390.

Schultz, D. M., and Coauthors, 2002: Understanding Utah winter storms: The Intermountain Precipitation Experiment. *Bull. Amer. Meteor. Soc.,* **83,** 189–210.

Sinclair, M. R., 1994: A diagnostic model for estimating orographic precipitation. *J. Appl. Meteor.,* **33,** 1163–1175.

Smith, R. B., 1979: The influence of mountains on the atmosphere. *Advances in Geophysics,* Vol. 21, Academic Press, 87–230.

——, 2003: A linear time-delay model of orographic precipitation. *J. Hydrol.,* **282,** 2–9.

——, 2004: Progress on the theory of orographic precipitation. *Tectonics, Climate and Landscape Evolution,* S. Willet, Ed., Geological Society of America, in press.

——, and I. Barstad, 2004: A linear theory of orographic precipitation. *J. Atmos. Sci.,* **61,** 1377–1391.

——, Q. F. Jiang, M. G. Fearon, P. Tabary, M. Dorninger, J. D. Doyle, and R. Benoit, 2003: Orographic precipitation and air mass transformation: An alpine example. *Quart. J. Roy. Meteor. Soc.,* **129B,** 433–454.

——, I. Barstad, and L. Bonneau, 2005: Orographic precipitation and Oregon's climate transition. *J. Atmos. Sci.,* **62,** 177–191.

Stensrud, D. J., and M. S. Wandishin, 2000: The correspondence ratio in forecast evaluation. *Wea. Forecasting,* **15,** 593–602.

White, A. B., P. J. Neiman, F. M. Ralph, D. E. Kingsmill, and P. O. G. Persson, 2003: Coastal orographic rainfall processes observed by radar during the California Land-Falling Jets Experiments. *J. Hydrometer.,* **4,** 264–282.

Wilks, D. S., 1995: *Statistical Methods in the Atmospheric Sciences.* Academic Press, 467 pp.

Yang, D., and Coauthors, 1998: Accuracy of NWS 8" standard nonrecording precipitation gauge: Results and application of WMO intercomparison. *J. Atmos. Oceanic Technol.,* **15,** 54–68.

Yuter, S. E., and R. A. Houze, 2003: Microphysical modes of precipitation growth determined by S-band vertically pointing radar in orographic precipitation during MAP. *Quart. J. Roy. Meteor. Soc.,* **129B,** 455–476.